Elsevier Editorial System(tm) for
Engineering Structures

Manuscript Draft

Manuscript Number: ENGSTRUCT-D-16-00354R1

Title: Mechano-electrochemical modelling of corroded steel structures

Article Type: Research Paper

Keywords: finite element method; effects of strain; corrosion; welding

Corresponding Author: Dr. Yikun Wang, BSc, MSc, PhD

Corresponding Author's Institution: University of Southampton

First Author: Yikun Wang, BSc, MSc, PhD

Order of Authors: Yikun Wang, BSc, MSc, PhD; Julian A Wharton, BSc, PhD; R A Shenoi, BTech, PhD

Abstract: A numerical methodology is established to study the mechano-electrochemical performance of corroded steel structures under external and internal stresses. Results show that mechanical stimuli (elastic/plastic deformation) increase the local anodic current density, and thus the corrosion behavior dynamically responds to the loading conditions. The current density increment for a multi-component stress system is largely dependent on both hydrostatic pressure and equivalent plastic strain. Moreover, the mechano-electrochemical corrosion is more affected by plastic deformation, resulting in localized areas being more anodic. Existing corrosion introduces extra stress/strain concentration, which further reduces the structural strength capacity and intensifies the corrosion damage.

Mechano-electrochemical modelling of corroded steel structures

Commented [Y.1]: Reviewer #3

Y. Wang
Fluid Structure Interactions Group, Civil, Maritime and Environmental Engineering and Science
University of Southampton
Boldrewood Innovation Campus
Southampton, SO16 7QF
United Kingdom
Email: yw4u14@soton.ac.uk

J.A. Wharton
National Centre for Advanced Tribology at Southampton (nCATS), Engineering Sciences
University of Southampton
Highfield Campus
Southampton, SO17 1BJ
United Kingdom

R.A. Shenoi
Southampton Marine and Maritime Institute,
University of Southampton
Boldrewood Innovation Campus
Southampton, SO16 7QF
United Kingdom

ABSTRACT

A numerical methodology is established to study the mechano-electrochemical performance of corroded steel structures under external and internal stresses. Results show that mechanical stimuli (elastic/plastic deformation) increase the local anodic current density, and thus the corrosion behavior dynamically responds to the loading conditions. The current density increment for a multi-component stress system is largely dependent on both hydrostatic pressure and equivalent plastic strain. Moreover, the mechano-electrochemical corrosion is more affected by plastic deformation, resulting in localized areas being more anodic. Existing corrosion introduces extra stress/strain concentration, which further reduces the structural strength capacity and intensifies the ~~mechano-chemical~~ corrosion damage.

Commented [Y.2]: Reviewer #4

Keywords: steel; finite element method; effects of strain; corrosion; welding.

NOMENCLATURE

$\bar{\alpha}$	Coefficient describing of mobile dislocation density dependence on strain (10^9 to 10^{11}) / cm^{-2}
β	Slenderness ratio
$\Delta\gamma$	Plastic shearing strain
$\Delta\varepsilon$	Macro plastic strain
ν	Poisson's ratio
σ_m	Absolute value of the spherical stress in the solid phase / MPa
σ_y	Yield stress of the material / MPa
$\Delta\tau$	Hardening / MPa
υ	Orientation-dependent factor
$\Delta\varphi_{Total}$	Total change in the equilibrium potential of a stressed electrode / V
$\Delta\varphi_e$	Change in the equilibrium potential of an elastically stressed electrode / V
$\Delta\varphi_p$	Change in the equilibrium potential of a plastically stressed electrode / V

a	Plate length / mm
b	Plate width / mm
b_f	Flange width / mm
B	Width between two longitudinal girders / mm
E	Young's modulus / GPa
E_t	Tangent modulus / GPa
F	Faraday constant / C mol^{-1}
h_w	Web height / mm
i_a	Anodic current density of a stressed electrode / A m^{-2}
i_{a0}	Anodic current density of a non-stressed electrode / A m^{-2}
k_d	Boltzmann constant for a system of particles representing unit dislocations / J K^{-1} cm
ΔN	Increase in the dislocation density at the hardening / cm^{-2}
N_0	Dislocation density when no hardening / cm^{-2}
N_{max}	Maximum possible dislocation density / cm^{-2}
n	Number of dislocation in planar pile-ups
R	Gas constant / J mol^{-1} K^{-1}
t	Original plate thickness / mm
t_f	Flange thickness / mm
t_{gc}	Remaining thickness due to grooving corrosion / mm
t_p	Thickness reduction due to pitting corrosion / mm
t_w	Web thickness / mm
T	Absolute temperature / K
V_m	Molar volume / m^3 mol^{-1}
w_c	Column-type initial deflection / mm
w_{gc}	Width of grooving corrosion / mm

w_{pl}	Plate initial deflection / mm
w_s	Sideways initial deflection / mm
z	Number of electrons within the partial electrochemical reaction

1. INTRODUCTION

In the context of ship and offshore structures, the initiation and progression of marine corrosion may be related to various types of mechanisms, such as galvanic corrosion, integranular corrosion, crevice corrosion and erosion corrosion [1]. Depending on the age of the structure, corrosion protection system and the environmental factors, the corrosion process can be dominated by one or more mechanisms [2-4]. Particularly, the combined mechanical and corrosion influence is often termed ~~mechano-chemical or~~ mechano-electrochemical changes in physico-mechanical properties of a solid surface [5]. Previous studies have focused on stress corrosion cracking [6, 7], corrosion fatigue [8-10] and hydrogen-induced cracking [11-13] and erosion-corrosion [14-16]. It has been reported that 23-33% of the low-alloy steel weight loss was attributed to the mechano-electrochemical effects, while the number could be 55-62% for austenitic stainless steels [17]. Various experiments and simulations along with theoretical/empirical formulas have been proposed to establish the relationship between stress/strain and the corrosion behavior. However, the conclusions are largely dependent on the metallurgic characteristics of the material and the test environments. In consequence, the synergistic effect of mechanical factors and electrochemical processes remain poorly understood.

An early study carried out by Despic et al. [11] in 1968 reported that during corrosion, only the rate of hydrogen evolution was affected by tensile elastic stress. The chemical potential (the partial molar free Gibbs energy of a substance) of hydrogen was believed to decrease under stress, which lowered the activation energy barrier for hydrogen-metal discharge and hence enhanced the cathodic reaction. Conversely, Gutman concluded that both tensile and compressive elastic stress would equally and directly affect the anodic reaction by increasing the surface chemical potential and reducing the equilibrium potential [5]. Similar conclusions were drawn in Ref [18]. Generally the influence of elastic stress may vary significantly but is often reported to be limited in magnitude (less than 1 mV [19]). Although care must be taken since the reported measurement provides a total or average value for the entire specimen and may not be representative of the actual conditions which may be present at localized sites [20]. Investigations of plastic deformation effects have been carried out by applying external loading, cold work or welding, which leads to direct and/or residual plastic strain. Under external load, it has been

Commented [WY3]: Reviewer #2 Comment 1

Commented [WY4]: Reviewer #2 Comment 5

Commented [Y.5]: Reviewer #4

Commented [Y.6]: Reviewer #4

Commented [Y.7]: Reviewer #4

generally agreed that the plastic strain will significantly reduce the corrosion resistance by directly enhancing the anodic reaction [7, 11, 14, 16, 21-26] while the hydrogen evolution was reported to increase as well [21, 22]. Despic et al. [11] observed that a negative corrosion potential shifted by up to 30 times, with a marked increase in the anodic current density at the onset of the tensile plastic strain and reached an asymptotic value gradually. Plastic deformation was believed to increase the surface reactivity non-uniformly [26] and the stored energy within a material, which can be directly related to the electrode potential change [27]. The increased current density at an early stage of cold rolling and a decreased value in the dynamic recovery stage of the hardening process corroborated the observations under external loading [28]. In terms of welds, electrochemically more negative potentials have been detected in the vicinity of weld boundary using either a micro-capillary probe or Kelvin probe [5, 29, 30]. The relatively high potential on the weld bead was reported to be induced by a thick oxide film [30] as well as a lower residual stress in comparison to the base metal [5]. More recently, due to the increase in the computational capability, research of mechano-electrochemistry has been achieved numerically with implementation of Gutman's formulas [5] to provide more detailed information on the corrosion enhancement [31, 32].

Regarding corrosion on marine structures (ships and offshore platforms/pipelines), large-scale pitting and grooving corrosion are considered to be major forms of localized damage [33], which has a more significant impact on the structural resilience compared to uniform/general corrosion [34, 35]. Pitting is frequently associated with coating breakdown or ineffective cathodic protection, which leads to pits that are tens of millimeters in diameter. Figure 1 shows a 3D surface profilometry of typical pitting damage on the inner bottom plating of a 15 to 16 years old bulk carrier, where broad pits with vertical walls can be easily observed (Figure 1 (b)). At the weld joints of large steel panels, grooving corrosion (also referred to as preferential weld line, knife-line or trench-like corrosion) may occur, which is a selective and rapid corrosion along a weld joint [33, 36]. The mechanisms of grooving corrosion is considered to be a much more complex situation. Indeed it has been previously reported that galvanic effects arise from differences within the metallographic structures (welds, heat affected zone (HAZ) and the base metal) and/or the inclusion of MnS stringers [36]. Also, weld imperfections (spatter) subsequently mean a thickness fluctuation of an applied protective coating, and hence exacerbate the corrosion. For both corrosion types, experiments have showed that the deformation/flexure of structures in service would inevitably result in protective layer (coating and/or rust) flake-off and hence an accelerated damage in the long term [37]. And last but not least, the in-service stresses and the above mentioned weld-induced residual stresses may have a significant influence on the surface chemical state [5]. General practices in assessing the corrosion condition in aged marine structures can be found in Ref [38].

Commented [WY8]: Reviewer #4

Commented [WY9]: Reviewer #4

Commented [WY10]: Reviewer #3 Comment 10

Commented [WY11]: Reviewer #2 Comment 5

Commented [Y.12]: Reviewer #2 Comment 3

Commented [Y.13]: Reviewer #4

Commented [Y.14]: Reviewer #3 Comment 1

Commented [WY15]: Reviewer #2 Comment 3

Commented [WY16]: Reviewer #3 Comment 2

Commented [WY17]: Reviewer #2 Comment 5

A marine structural system will endure various loading throughout its lifetime. Within the system, which is often consisting of a number of different structural members, some members will always reach their collapse or ultimate strength first before the whole system collapses. Thus, taking into account the ultimate strength and post-collapse behavior of individual structural members is essential to determine the overall integrity of a structural system. There has been significant effort to assess the strength capacity of steel marine structures with uniform corrosion [39, 40] and localized corrosion damage using both experimental and finite element (FE) methods [34, 41], varying structural geometries, corrosion extent, loading/boundary conditions and structural initial imperfections. While the influence of pitting corrosion has been investigated in depth over the last decade [42-46], grooving corrosion has gained increasing attention only recently [47-49]. Considering that both corrosion types will result in stress/strain concentrations, however, only a limited number of studies have addressed the mechanically assisted reactions on the corrosion performance of marine structures loaded to an ultimate condition. In addition, the frequently used Gutman method needs to be appropriately considered for structures in a multi-component stress state. This paper studies the mechanical and mechano-electrochemical performance of steel structures subjected to localized corrosion damage (assuming charge transfer control and neglecting the presence of protective coatings or oxide layers), using previously constructed pitting and grooving FE models [45, 48] in order to predict corrosion acceleration at 'hot spot' locations induced by stress/strain effects and to quantify the corrosion enhancement.

Commented [WY18]: Reviewer #2 Comment 5

Commented [Y.19]: Reviewer #2 Comment 3

Commented [Y.20]: Reviewer #3 Comment 17

2. METHODOLOGY

FE analysis was conducted using ANSYS 14.0 as a primary tool to achieve material and geometric nonlinearities using bilinear isotropic hardening and large deflection options [50]. To assess the influence of corrosion features, this study has examined a square plate with pitting corrosion features and a simplified stiffened plate model with grooving corrosion features, as typical representatives of a deck or bottom plating of a double hull oil tanker. The geometric and material properties for the two models are listed in Table 1. A 4-node shell element SHELL181 was adopted for the plate model and an 8-node solid element SOLID185 together with a contact element couple was chosen for the stiffened plate in order to construct a realistic fillet weld connection within the FE model. The maximum element size for the plate model was 16 mm while the element size ranged from 3 mm to 47.5 mm. Equations shown in Table 1 were assigned for each nodal coordinates for the initial deflection applications. The four edges of each model were simply supported with a compressive load applied in the longitudinal direction by controlling

Commented [WY21]: Reviewer #3 Comment 3

the displacement. A full description of the weld modelling, the convergence study for element size selection and boundary conditions can be found in detail elsewhere [45, 48]. The von Mises criterion was used to assess yielding. Regarding the stiffened plate model, a widely used weld-induced residual stress distribution was explicitly applied in the longitudinal direction, where the tensile stress in HAZ reaches the yield stress of the material while an average level of compressive stress ($-0.15\sigma_y$) was assigned for the unaffected area [51]. Specifically, based on residual stress distribution, a matrix was formed consisting of stress records for every integration point in every element depending on the location of the element centroid. After the application of the initial deflection, the initial stress matrix was read and solved with all degrees of freedom constrained in order to obtain the reaction force records for all elements. The constraints were then cleared up and replaced with the real boundary conditions, followed by a calculation procedure with two load steps. The initial stress matrix and the reaction force matrix were read again in the first step for the residual stress application. The external load was subsequently added for the ultimate strength analysis. Validation of the nonlinear FE method, as well as the residual stress application, have been conducted with good correlations achieved in both pre- and post-ultimate strength regimes [45, 48], see for example Figure 2 for a 800 mm × 800 mm × 15 mm plate with regularly distributed cylindrical pits (DOP = 0 (intact), 4.91%, 9.6%, 15.9%, 23.75% and 33.2%; pit depth = 7.5 mm).

Commented [WY22]: Reviewer #3 Comment 3

Commented [Y.23]: Reviewer #3 Comment 4

For the plate models, two idealized localized pit distributions on one side of the plate were considered, as shown in Figure 3 with typical mesh patterns. Five degrees of pitting (DOP, which is the ratio of damaged area to the plate surface area) (2%, 5%, 10%, 15% and 25%) and four thickness reductions, t_p ($0.2t$, $0.25t$, $0.33t$ and $0.5t$, where t is the original plate thickness), were investigated. Regarding the stiffened plate model, grooving corrosion was located on both sides of the stiffener (Figure 4 (a)) with the groove width w_{gc} varying between 5%h_w and 50%h_w, and the remaining thickness t_{gc} of $0.25t_w$, $0.5t_w$ and $0.75t_w$ (where h_w is the stiffener web height and t_w is the original stiffener web thickness). Contact elements TARGE170 coupled with CONTA175 were adopted in this investigation to represent the fillet weld connections [50] (Figure 4 (b)). For the interface between the stiffener and the plating, Coulomb's friction model was used with the static coefficient of friction of 0.78 and a dynamic value of 0.42 for a high-tensile steel contact [48].

Based on Gutman's theory [5], when a solid surface is elastically stressed, the chemical potential of an atom of a solid is determined by the spherical part of the macroscopic stress tensor, i.e., the hydrostatic pressure, and hence leading to increases in macroscopic chemical potential in the solid surface. In turn, this will result in a decrease in the equilibrium potential (Equation 1) [5].

Commented [Y.24]: Reviewer #3 Comment 7

$$\Delta\varphi_{\mathrm{e}} = -\frac{\sigma_{\mathrm{m}} V_{\mathrm{m}}}{zF} \tag{1}$$

where $\Delta\varphi_{\mathrm{e}}$ is the change in equilibrium potential (V). σ_{m} is the absolute value of the spherical stress in the solid phase (MPa), V_{m} is the molar volume ($\mathrm{m^3\ mol^{-1}}$), z is the number of electrons within the partial electrochemical reaction and F is the Faraday constant. When considering metal dissolution, only the anodic current density is directly affected by the mechano-electrochemical action [5].

Commented [Y.25]: Reviewer #3 Comment 7

$$i_{\mathrm{a}} = i_{\mathrm{a0}} \exp\frac{\sigma_{\mathrm{m}} V_{\mathrm{m}}}{RT} \tag{2}$$

where i_{a0} is the anodic current density of a non-stressed electrode ($\mathrm{A\ m^{-2}}$); R is the ideal gas constant and T is the temperature (K). With further increases in the applied load, a local change in the equilibrium potential induced by plastic deformation can be expressed as follows [5].

Commented [Y.26]: Reviewer #3 Comment 6

Commented [Y.27]: Reviewer #3 Comment 7

$$\Delta\varphi_{\mathrm{p}} = -\frac{n\Delta\tau R}{\bar{\alpha} k_{\mathrm{d}} N_{\max} zF} \tag{3}$$

where n is the number of dislocation in planar pile-ups; $\bar{\alpha}$ is between 10^9 and 10^{11} $\mathrm{cm^{-2}}$ [5]; k_{d} is the Boltzmann constant for a system of particles representing unit dislocations and $N_{\max}$ is the maximum possible dislocation density. The plastic deformation is realised as micro shear strain $\Delta\gamma$ and the increase in the dislocation density ΔN ($\mathrm{cm^{-2}}$) with hardening stress $\Delta\tau$ (MPa) is [5].

Commented [Y.28]: Reviewer #3 Comment 7

$$\Delta N = N_0 \left(\exp\frac{n\Delta\tau}{\bar{\alpha} k_{\mathrm{d}} N_{\max} T} - 1\right) \tag{4}$$

where N_0 is the dislocation density ($\mathrm{cm^{-2}}$) at $\Delta\tau = 0$ (approximately 10^8 $\mathrm{cm^{-2}}$ [5]). Thus, the macro plastic strain can be expressed as [5].

Commented [Y.29]: Reviewer #3 Comment 7

$$\Delta\varepsilon = \frac{\Delta\gamma}{\upsilon} = \frac{N_0}{\bar{\alpha}\upsilon}\left(\exp\frac{n\Delta\tau}{\bar{\alpha} k_{\mathrm{d}} N_{\max} T} - 1\right) \tag{5}$$

where υ is the orientation-dependent factor (which is equal to 0.45 for tensile condition [5]). If a steel structure is loaded until it reaches its ultimate strength with plasticity occurring to a certain extent and left

under stress, the overall increase in the equilibrium potential of the structure surface should be the summation of the elastic and plastic effects. By taking into account Equations 4 and 5, the local anodic current density is [5].

$$i_a = i_{a0}\exp\frac{\sigma_m V_m}{RT}\left(\frac{\Delta\varepsilon}{\varepsilon_0}+1\right) \quad (6)$$

where ε_0 represents the onset of plastic strain. From Equation 6 it can be seen that the contribution of mechanical stress to the potential or current change should consist of the spherical part of the applied stress and the plastic strain. By substituting $V_m = 7.09 \times 10^{-6}$ m^3 mol^{-1} for iron and $\varepsilon_0 = \sigma_y/E$, the ratio of the local anodic current density of a stressed structure to the unstressed condition can be estimated. It needs to be emphasised that when a solid is experiencing a multi-component elasto-plastic stress state due to an out-of-plane deformation, $\Delta\varepsilon$ cannot be taken as the axial plastic strain even though the external loading is uniaxial. Since the von Mises criterion was used to judge the onset of yielding, the plastic strain will only be developed when the equivalent (von Mises) stress is equal to the yielding stress of the material. The concept of equivalent stress/strain is used as a scalar value to simplify the stress state to the uniaxial condition by keeping the unit distortion strain energy the same. Therefore, $\Delta\varepsilon$ was treated as the equivalent plastic strain for this study. It was assumed that the structural surface was anodic and the structural members were located in a cargo oil tank, where the average temperature was set to be 60°C. The corrosion process was charge transfer controlled due to the very low oxygen level (below 5%) and highly acidic environment (pH = 0.85) [52, 53]. The influence of a polymeric coating was not considered. When the plate was loaded up to the ultimate strength stage, both the hydrostatic stress σ_m and the equivalent plastic strain $\Delta\varepsilon$ were readily obtained for every element from the FE model. Utilizing Equation 6, the anodic current density increment ratio (i_a/i_{a0}) can be calculated.

Scanning Kelvin Probe Force Microscopy (SKPFM) was performed on a representative welded steel plate. Four square specimens (25 mm × 25 mm × 6 mm) were fabricated from a multi-pass butt welded steel plate (Grade 070M20 for marine applications), as shown in Figure 5. MIG wire EN 440 was used for the welding (deposits C – 1.3% Mn weld metal with a copper coat finish and double deoxidized). The welding temperature was between 1200℃ and 1300℃, at a speed of 100 mm min^{-1}. The material is widely used for welding low carbon, low alloy steel structures, ship grade steels (A, B, D and E) and equivalent mild steels. Moreover, it is frequently utilized especially for thin plates of ship structures, container buildings, bridges, railway constructions and pressure vessels. Prior to the SKPFM tests, chemical surface cleaning was conducted according to the standard practice ASTM (G1-03) by dipping

Commented [Y.30]: Reviewer #3 Comment 7

Commented [Y.31]: Reviewer #3 Comment 8

Commented [WY32]: Reviewer #4

Commented [Y.33]: Reviewer #3 Comment 9

Commented [Y.34]: Reviewer #3 Comment 10

the sample surfaces into a 1000 mL pickling solution (500 mL 37% HCl, 3.5 g hexamethylenetetramine and deionized water) at room temperature for 10 minutes. No mechanical/chemical polishing was carried out due to its potential influence on the residual stresses and the surface state. Samples were stored in a desiccator before testing. The SKPFM was performed using atomic force microscopy (AFM) (MAC Mode III, 5500 Scanning Probe Microscopy, Agilent Technologies, US). PicoView 1.12 and PicoImage Basics 6.0 (Agilent Technologies, US) software were used for data acquisition and image analysis, respectively. Conducting AFM probes, OMCL-AC240TS (from Olympus) with nominal spring constant ~ 2 N m^{-1} were used. Image sizes of 1 × 1 μm^2 were recorded with a resolution of 512 lines at scan rate 2 lines s^{-1}. Measurements were done along the *y*-axis (Figure 5) of the sample every 3 to 5 mm. Topography and surface potential measurements were performed simultaneously in amplitude modulation mode in an environmental chamber. The Volta potential difference between the sample surface and the AFM tip surface was calculated by averaging the potential signal over the whole scan area. As all measurements were performed in air, the effect of oxygen contamination cannot be excluded. More details on SKPFM technique can be found in Refs. [54, 55].

3. RESULTS

3.1 Plate models with pitting corrosion features

An external compressive load was applied in numerous substeps until the model reached the ultimate strength state (collapse). The procedure to obtain the stress/strain progress and the ultimate strength degradation are presented in Ref. [45]. Figure 6 shows an example of the anodic current density increment ratio (i_a/i_{a0}) distribution for a plate with random pitting corrosion (DOP = 15%, pit depth = $0.2t$) at two load substeps ($0.43\sigma_y$ and $0.65\sigma_y$) for a charge transfer controlled corrosion process at 60°C. When the load was relatively low ($0.43\sigma_y$), most of the plate area remained elastic (Figure 6 (a)). It can be seen that the anodic current density ratio increased slightly (approximately 1.3 times) and mainly occurs in the middle of the plate and along the four edges. When the load was increased to $0.65\sigma_y$, which equals the ultimate strength of the model (Figure 6 (b)), the current density ratio increased markedly (1.5 to 4 times) compared to the unstressed condition, concentrated on the middle area and the unloaded edges. Similar distributions have also been observed for intact plates, as well as plates with a large corrosion feature in the middle. Examining the cross-sectional area along the unloaded edge, as shown in Figure 6 (c) and (d), it can be seen that high current density ratio emerges around the pit edges initially and gradually develops on the bottom of the pits. Moreover, the interactions between the random pits were enhanced as the load increased.

Commented [Y.35]: Reviewer #3 Comment 11

Commented [Y.36]: Reviewer #3 Comment 12

To better understand the mechano-electrochemical behavior of the plate models, Figure 7 provides results of hydrostatic pressure, equivalent plastic strain and anodic current density increment ratio for 15% DOP and four pit depths along the plate mid-section with a relatively large corrosion feature in the middle at the ultimate strength stage. The geometric discontinuity induced by the corrosion defect largely influences the stress/strain values inside and adjacent to the pit edge. As the pit depth increases (from $0.2t$ to $0.5t$), the hydrostatic pressure shows minor variation in the maximum value in the middle of the plate but a sudden drop at the damage boundaries. Compared to the intact plate, the equivalent plastic strain reaches a maximum value at the boundary of the damage. As the corrosion damage becomes deeper, it is interesting to note that the strain inside the pit increases accordingly, whereas the value decreases outside the pit. In addition, variation starts to emerge inside the pitted area. The distribution of the anodic current density change follows a similar trend as the plastic strain results. When the corrosion depth is increased to $0.5t$, the location with the highest current density increase moves from the damage boundary towards the centre. However, the profile of the results showed no significant change during the loading process (Figure 8 with the load varying from $0.6\sigma_y$ to its ultimate strength). When examining the influence of DOP (Figure 9), it was found that for the same corrosion depth, as DOP increased, the current density change inside the pit approached the intact condition while the values outside the damage decreased.

3.2 Stiffened plate models with grooving corrosion features

Firstly, for the stiffened plate model, a study was carried out for an unstressed intact condition. Figure 10 shows the influence of the longitudinal weld-induced residual stresses on the electrochemical properties. From the anodic current density ratio plot (Figure 10 (a)) it can be seen that a higher ratio occurs at the HAZ with maximum tensile stress. When further examining a cross-section A-A' (mid-section, half-width of the base metal from the weld boundary to the plate edge), the longitudinal stress and the equilibrium potential change, $\Delta\varphi_{\mathrm{Total}}$, on the plate surface are also obtained and plotted in Figure 10 (b). $\Delta\varphi_{\mathrm{Total}}$ is a summation of the elastic (Equation 1) and plastic (Equation 3) effects. It clearly shows that a significant decrease in potential corresponds to the change of the residual stress sign. Accordingly, Figure 11 presents the Volta potential difference between the sample surface and the AFM tip surface, across the butt weld and the adjacent plate surface profile (Figure 5). The Volta potential difference has its highest value (approximately 0.143 V) at the weld center and decreases to 0.006 V at 55 mm from the centerline. Further away from the weld the Volta potential difference stabilizes at around 0.012 V. For the base metal area, the 6 mV potential difference between the steel plate and HAZ is comparable with the results obtained from the modelling (3 to 4 mV) shown in Figure 10 (b).

Commented [Y.37]: Reviewer #3 Comment 13

Commented [Y.38]: Reviewer #3 Comment 14

As the structure deforms, a continuous redistribution of the anodic current density has been observed for all conditions during the loading process. Based on the stress/strain relationship, an example of such redistribution is shown in Figure 12. At the first load substep (Point 1), when the model is elastically deformed, it can be seen that a slight increase in the current density increment ratio appears on the structure surface with the highest i_a/i_{a0} of approximately 1.6 at the corroded region. Regardless of the boundary constraint effect, when further increasing the load with a significant development of plasticity until collapse (Points 2 and 3), a marked rise in the current density occurs not only in the corroded area but also on the intact plate and the flange, mainly concentrated on the mid-section of the model.

Data were also extracted along the mid-section on both sides of the plate and the stiffener, as illustrated in Figure 4 (a) (Lines P_1-P_1', P_2-P_2', W_1-W_1' and W_2-W_2'). Figures 13 to 15 show results for a stiffened plate model at the ultimate strength stage with a fixed corrosion width (10% h_w) and varying the remaining thickness ($0.75t_w$, $0.5t_w$ and $0.25t_w$). For the surface of the plate in the intact model (Figure 13), the sign of hydrostatic pressure indicates that Line P_1-P_1' is under compression while P_2-P_2' is under tension (positive hydrostatic pressure). Conversely, the left side of the stiffener (W_1-W_1') is under tension (Figure 14) while the right side (W_2-W_2') is under compression (Figure 15). The presence of grooving corrosion mainly affects the stress distribution on the stiffener surface, adding more compression to W_1-W_1' and easing the compressive stress on W_2-W_2'. The influence is much more significant inside the grooves as the corrosion becomes deeper. The equivalent plastic strain reaches its highest value on the plate adjacent to the weld joint. Much larger strain occurs inside the grooves compared to the intact condition with lower values outside the grooves. However, it is interesting to note that when the remaining thickness is only $0.25t_w$ minimal plastic strain develops inside the grooves at the mid-section location. In terms of the anodic current density ratio, similar distributions can be seen as the plastic strain for all locations, with maximum current density of 6 to 7 times higher at the corroded area than for the unstressed condition. ~~The results were also compared to models without weld-induced residual stresses. Similar distributions of the stress/strain values were obtained. However, the maximum current density was only 3 to 4 times higher than the unstressed surface and the plastic strain was greatest at the edge of the weld.~~

Commented [Y.39]: Reviewer #3 Comment 15

Commented [WY40]: Reviewer #3 Comment 16

4. DISCUSSION

From the mechano-electrochemical evaluation of simple plate models, it is evident that the locations of the stress/strain concentration are closely associated with the applied initial deflection and boundary

conditions. When the plates are elastically deformed, higher hydrostatic pressure develops in the middle and four corners of the plate, due to the shape of the initial deflection. The idealized corrosion features have added extra complexity to the stress distribution, which determines the anodic current density distribution at the elastic stage, as shown in Figure 6 (a). As the model further deforms, plastic strain starts to develop along the unloaded edges and propagates to the center (Figure 6 (b)), due to the development of the membrane stress in the central area. With the presence of corrosion damage, the highest plastic strain and i_a/i_{a0} always occur at the damage boundary initially (Figure 6 (c)), as also reported in Refs. [45, 46]. However, as the external load further increases, the strain and i_a/i_{a0} quickly increases at the bottom of the pits (Figure 6 (d)). This finding is of great importance since when plasticity has spread to a large extent on a structure, not only the area with geometric discontinuity but also the area adjacent to it become more anodic. The subsurface below the corrosion feature is therefore more likely to experience corrosion acceleration and corrosion-induced cracking.

From the results at half-length of the plate, Figure 7 clearly shows that the development of plastic strain plays a major role in altering the current change profile, leading to much higher values. In addition, at the ultimate strength stage, the corrosion damage results in a plastic strain increase inside the corroded area and a decrease in the surrounding intact area compared to the uncorroded condition (Figure 7 (b)). This phenomenon becomes more obvious as the pit depth increases, implying a more localized plastic strain distribution. This is due to the lower membrane tensile stress in the plate induced by corrosion damage, which leads to a less effective stress/strain redistribution in the plastic regime and a much increased local deformation. A similar distribution of equivalent stress has also been reported before, which is explained as stress concentration in the elastic region [32]. Ultimately, the concentrated hydrostatic pressure and the equivalent plastic strain lead to a more localized anodic current density increase, indicating that a more severe corrosion enhancement is expected at the corrosion site leaving the surrounding intact region less of an issue. The localized corrosion enhancement is also observed for small DOPs, as shown in Figure 9. However, when increasing DOP, the current density increment decreases both inside and outside the pit, due to a greater influence of the larger corrosion area on the stress/strain redistribution along the unloaded edges. It is noticeable that when the pit depth is up to $0.5t$, there is a profile change mainly in the plastic strain, leading to a much greater current density increase in the middle of the corroded region compared to the boundaries. This higher strain is primarily caused by the greatly reduced strain at the center of both unloaded edges in addition to the yielded intact area around the pit. However, for every DOP and corrosion depth, the distribution profile of the stress/strain and the current density remains unchanged during the loading process (Figure 8). Also, minor variation in the distribution shape is obtained for different DOPs, suggesting that the location of corrosion acceleration is largely determined by corrosion

depth instead of the external load or DOP. Thus, pit depth not only has a greater impact on the strength capacity reduction [45], but also the mechano-electrochemical performance.

The stiffened plate model investigation shows greater complexity due to the application of residual stresses, various initial deflections and the connection between the stiffener, weldment and plating. Specifically, the residual stresses in the longitudinal direction cause a negative potential shift (Figure 10 (b)) at the HAZ, which could potentially operate as active anodes, while the remainder with a less unchanged current value become cathodes. The potential variation was confirmed by the SKPFM measurements (Figure 11). However, compared to the slight potential change on the flat plate surface away from the weld, it can be seen that a more significant negative shift was detected at the weld boundary compared to the center of the weld (up to 0.1 V). A similar distribution was also reported in the literature from experiments [5, 29]. Clearly the SKPFM measurements show a much more complex picture compared to the modelling results (Figure 10 which again demonstrates that the mechanisms of grooving corrosion is a combination of mechanical effects, variance in the composition of the welds and the base metal and the altered microstructure, which ultimately leads to knife-line corrosion attack. From the electrochemical standpoint, the experimental result again rationalizes the location of the grooving corrosion in the stiffened plate models.

From Figure 12 it can be seen that the distribution of the changed anodic current density is not only dependent on the corrosion location but also affected by the structural deformation. As the external load increases, the increased mechano-electrochemical effect is more affected by the plastic behavior and becomes more localized along the weld joint, implying a smaller contribution of elastic deformation to the ~~mechano-chemical~~ corrosion behavior.

Commented [Y.41]: Reviewer #4

From Figures 13 to 15 it is apparent that weld-induced residual stresses not only enhance the mechano-electrochemical performance of corroded structures, but also cause stress/strain redistribution during the loading process, resulting in a much lower plastic strain along the welds on both sides of the plate. However, the low plastic strain inside the grooves when the remaining thickness is down to $0.25t_w$ was found to be induced by the change in the failure mode of the stiffener [48]. This phenomenon affects the difference in plastic strain distribution over the structural surface. For example, the plastic strain development for models with remaining web plate thickness of $0.75t_w$ and $0.25t_w$ (Figure 16) shows that plastic strain develops in the groove at the mid-section area for $0.75t_w$ but at the adjacent area for $0.25t_w$, which directly affects the mechano-electrochemical properties.

5. CONCLUSIONS

A numerical methodology has been proposed and developed to evaluate the mechano-electrochemical performance of locally corroded steel structures subjected to external loading and weld-induced residual stresses. At the ultimate strength state, for both plates and stiffened panels, the distribution of the mechano-electrochemical properties follows a similar profile as the plastic strain, resulting in highly localized areas being more susceptible to enhanced anodic dissolution. A change in the external load and/or the cross-sectional area of a structure could lead to a stress state change and alter the electrochemical behavior. In addition, the existing corrosion damage could introduce extra localized stress/strain, which intensifies the mechano-electrochemical corrosion.

More importantly, for corrosion inspection, the actual physical realization of either corrosion current or potential measurements can only provide an integration of these quantities over a surface, which will mask the identification of singular features in the vicinity of any damage. Likewise, there are limitations in specimen size and loading/boundary conditions within a laboratory. In comparison, FE modelling is shown here to be able to provide localized stress and strain information under a complex stress state. Although idealized in this study (with the exclusion of coatings and the simplified corrosion processes under specific loading and boundary conditions), the methodology proposed is considered to be able to identify the 'hot spot' locations of accelerated mechano-electrochemical corrosion and quantify the increased anodic current ratio. The utilization of this information could thus lead to more targeted corrosion inspections and optimized maintenance schedules, along with enhanced ship surveys. However, other factors such as the oxide film deformation due to the imposed stress/strain condition cannot be neglected. Further work is needed to investigate the changed surface state on future corrosion development and the strength capacity (ultimate strength) of a structure. Also, modelling of more realistic corrosion morphology using both numerical and physical sampling techniques is necessary to improve the accuracy of the FE predictions.

Commented [Y.42]: Reviewer #3 Comment 17

Commented [Y.43]: Reviewer #3 Comment 18

Commented [Y.44]: Reviewer #2 Comments 2, 4

ACKNOWLEDGEMENTS

The authors gratefully acknowledge the funding by the University of Southampton and The Lloyd's Register Educational Trust University Technology Centre (The LRET UTC). The authors would also like to thank Dr Jurgita Zekonyte for undertaking the SKPFM measurements.

REFERENCES

[1] Paik JK, Thayamballi AK. Chapter 10. Corrosion Assessment and Management. Ship-Shaped Offshore Installations: Design, Building, and Operation: Cambridge University Press; 2007.
[2] Melchers RE. Development of new applied models for steel corrosion in marine applications including shipping. Ships and Offshore Structures. 2008;3:135-44.
[3] Melchers RE, Jiang X. Estimation of models for durability of epoxy coatings in water ballst tanks. Ships and Offshore Structures. 2006;1:61-70.
[4] Shehadeh M, Hassan I. Study of sacrificial cathodic protection on marine structures in sea and fresh water in relation to flow conditions. Ships and Offshore Structures. 2013;8:102-10.
[5] Gutman EM. Mechanochemistry of solid surfaces. Singapore: World Scientific Publishing Co. Pte. Ltd.; 1994.
[6] Chu W, Ma R, Hsiao C. Stress corrosion cracking of mild streel under compressive stress. National Association of Corrosion Engineers. 1987;43:251-4.
[7] Liu X, Frankel GS. Effects of compressive stress on localised corrosion in AA2024-T3. Corrosion Science. 2006;48:3309-29.
[8] Pan T. Corrosion behaviour of a duplex stainless steel under cyclic loading: a scanning Kelvin probe force microscopy (SKPFM). Journal of Applied Elctrochemistry. 2012;2012:1049-56.
[9] Amiri M, Arcari A, Airoldi L, Naderi M, Iyyer N. A continuum damage mechanics model for pit-to-crack transitionin AA2024-T3. Corrosion Science. 2015;98:678-87.
[10] Burns JT, Larsen JM, Gangloff RP. Driving forces for localized corrosion-to-fatigue crack transition in Al–Zn–Mg–Cu. Fatigue & Fracture of Engineering Materials & Structures. 2011;34:745-73.
[11] Despic AR, Raicheff RG, Bockris JOM. Mechanism of the acceleration of the electrodic dissolution of metals during yielding under stress. The Journal of Chemical Physics. 1968;49:926-38.
[12] Migai LL, Vedeneeva MA, Zhuk NP. Effect of deformation on the corrosion resistance of steel Kh18N10T. Chemical and Petroleum Engineering. 1971;7:133-6.
[13] Lu BT, Yu H, Luo JL. Effects of plastic deformation and carbon dioxide on corrosion of pipeline steel in near-neutral pH groundwater. Journal of Materials Engineering and Performance. 2013;22:1430-5.
[14] Lu BT, Luo JL. Synergism of electrochemical and mechanical factors in erosion-corrosion. Journal of Physical Chemistry B. 2006;110:4217-31.
[15] Xie J, Alpas AT, Northwood DO. Mechano-electrochemical effect between erosion and corrosion. Journal of Materials Science. 2003;38:4849-56.
[16] Matsumura M, Oka Y, Hiura H, Yano M. The role of passivating film in preventing slurry erosion-corrosion of austenitic stainless steel. The Iron and Steel Institute of Japan International. 1991;31:168-76.

[17] Madsen BW. Measurement of erosion-corrosion synergism with a slurry wear test apparatus. Wear. 1988;123:127-42.
[18] Zhang S, Pang X, Wang Y, Gao K. Corrosion behavior of steel with different microstructures under various elastic loading conditions. Corrosion Science. 2013;75:293-9.
[19] Nobe K, Tan S. Electrical Potential Responses of Silver, Steel and Brass Stressed in Tension In Sodium Chloride Solutions. Corrosion. 1962;18:391t-5t.
[20] Harwood JJ. The influence of stress on corrosion. Corrosion. 1950;6:249-59.
[21] Movchan TG, Esipova NE, Eryukin PV, Uriev NB, Rusanov AI. Mechanochemical effects in processes of corrosion of metals. Russian Journal of General Chemistry. 2005;75:1681-6.
[22] Gutman EM, Solovioff G, Eliezer D. The mechanochemical behaviour of type 316L stainless steel. Corrosion Science. 1996;38:1141-5.
[23] Bonora PL, Andrei M, Eliezer A, Gutman EM. Corrosion behaviour of stressed magnesium alloys. Corrosion Science. 2002;44:729-49.
[24] Li W, Li DY. Variations of work function and corrosion behaviours of deformed copper surfaces. Applied Surface Science. 2005;240:388-95.
[25] Ren C, Zeng D, Lin J, Shi T, Chen W. Sour corrosion of c110 steel and its influence by galvanic couple and stress. Industrial & Engineering Chemistry Research. 2012;51:4894-904.
[26] Zhu Y, Li L, Wang C, Luo J, Gao G, Zhang J. Effects of elastic deformation on the anodic dissolution of X70 carbon steel in sulfuric acid solution. Electrochimica Acta. 2012;78:609-14.
[27] Lewis D, Northwood DO, Pearce CE. A study of the effects of microstrain on the electrode potential and the anodic dissolution of Cu. Corrosion Science. 1969;9:779-87.
[28] Peguet L, Malki B, Baroux B. Influence of cold working on the pitting corrosion resistance of stainless steels. Corrosion Science. 2007;49:1933-48.
[29] Han LT, Mansfeld F. Scanning Kelvin probe analysis of welded stainless steel. Corrosion Science. 1997;39:199-202.
[30] Bäck G, Nazarov A, Thierry D. Localised corrosion of heat-treated and welded stainless steel studied using a scanning Kelvin probe. Corrosion. 2005;61:951-60.
[31] Xu LY, Cheng YF. Corrosion of X100 pipeline steel under plastic strain in a neutral pH bicarbonate solution. Corrosion Science. 2012;64:145-52.
[32] Xu LY, Cheng YF. Development of a finite element model for simulation and prediction of mechanoelectrochemical effect of pipeline corrosion. Corrosion Science. 2013;73:150-60.
[33] DNV. Allowable thickness diminution for hull structure. Classification Notes -No. 72.1. Hovik, Norway 2013 (https://rules.dnvgl.com/docs/pdf/DNV/cn/2013-07/Cn72-1.pdf. Accessed on 07/07/2016) .
[34] Wang Y, Wharton JA, Shenoi RA. Ultimate strength analysis of aged steel-plated structures exposed to marine corrosion damage: A review. Corrosion Science. 2014;86:42-60.
[35] Comanescu I, Melchers RE, Taxén C. Corrosion and durability of offshore steel water injection pipelines. Ships and Offshore Structures. 2016;11:424-37.
[36] Kato C, Otoguro Y, Kado S, Hisamatsu Y. Grooving corrosion electric resistance welded steel pipe in sea water. Corrosion Science. 1978;18:61-74.
[37] Melchers RE, Paik JK. Effect of flexure on rusting of ship's steel plating. Ships and Offshore Structures. 2010;5:25-31.
[38] Rizzo CM, Paik JK, Brennan F, Carlsen CA, Daley C, Garbatov Y et al. Current practices and recent advances in condition assessment of aged ships. Ships and Offshore Structures. 2007;2:261-71.
[39] Kim DK, Kim SJ, Kim HB, Zhang XM, Li CG, Paik JK. Ultimate strength performance of bulk carriers with various corrosion additions. Ships and Offshore Structures. 2015;10:59-78.
[40] Bai Y, Kim Y, Yan H, Song X, Jiang H. Reassessment of the jacket structure due to uniform corrosion damage. Ships and Offshore Structures. 2016;11:105-12.

[41] Hairil Mohd M, Lee BJ, Cui Y, Paik JK. Residual strength of corroded subsea pipelines subject to combined internal pressure and bending moment. Ships and Offshore Structures. 2016;10:554-64.
[42] Paik JK, Lee JM, Ko MJ. Ultimate compressive strength of plate elements with pit corrosion wastage Proceedings of the Institution of Mechanical Engineers, Part M: Journal of Engineering for the Maritime Environment. 2003;217:185-200.
[43] Nakai T, Matsushita H, Yamamoto N, Arai H. Effect of pitting corrosion on local strength of hold frames of bulk carriers (1st report). Marine Structures. 2004;17:403-32.
[44] Huang Y, Zhang Y, Liu G, Zhang Q. Ultimate strength assessment of hull structural plate with pitting corrosion damnification under biaxial compression. Ocean Engineering. 2010;37:1503-12.
[45] Wang Y, Wharton JA, Shenoi RA. Influence of localised pit distribution and bench-shape pits on the ultimate compressive strength of steel plating for shipping. CORROSION. 2014;70:915-27.
[46] Sultana S, Wang Y, Sobey AJ, Wharton JA, Shenoi RA. Influence of corrosion on the ultimate compressive strength of steel plates and stiffened panels. Thin-Walled Structures. 2015;96:95-104.
[47] Khurram N, Sasaki E, Katsuchi H, Yamada H. Finite element investigation of shear capacity of locally corroded end panel of steel plate girder. International Journal of Steel Structures. 2013;13:623-33.
[48] Wang Y, Wharton JA, Shenoi RA. Ultimate strength assessment of steel stiffened plate structures with grooving corrosion damage. Engineering Structures. 2015;94:29-42.
[49] Khurram N, Sasaki E, Akmal U, Saleem MU, Amin MN. A comparative study in utilizing the shell and solid elements formulation for local corrosion simulation at bearing stiffener. Arabian Journal for Science and Engineering. 2016; 1-13 (doi:10.1007/s13369-015-2018-x).
[50] 14.0 A. Mechanical Applications. SAS IP, Inc; 2011.
[51] ISSC. Report of Specialist Committee III.1 Ultimate Strength. Proceedings of the 18th International Ship and Offshore Structures Congress. Rostock, Germany2012. p. 285-363.
[52] Hao X, Dong J, Etim IN, Wei J, Ke W. Sustained effect of remaining cementite on the corrosion behavior of ferrite-pearlite steel under the simulated bottom plate environment of cargo oil tank. Corrosion Science. 2016;110:296-304.
[53] IMO. Performance standard for alternative means of corrosion protection for cargo oil tanks of crude oil tankers. Resolution, MSC. 289(87) 2010.
[54] Berger R, Butt H, Retschke MB, Weber SAL. Electrical modes in scanning probe microscopy. Macromolecular Rapid Communications 2009;30:1167-78.
[55] Melitz W, Shen J, Kummel AC, Lee S. Kelvin probe force microscopy and its application. Surface Science Reports. 2011;66:1-27.

FIGURE CAPTIONS

Figure 1: Surface profilometry of a broad pit feature found on the inner bottom plating of an aged bulk carrier: (a) two-dimensional top view; (b) three-dimensional view of the pit along the direction of the arrow in (a). Scan area: 6 cm × 4 cm.

Figure 2: FE modelled compressive stress strain relationship (a) validated results; against (b) results obtained by Paik et al. [1].

Figure 3: Localized pit distributions: (a) random pitting (pit radii = 10 mm to 30 mm); (b) a single large corrosion feature in the middle (170 mm radius).

Figure 4: Stiffened plate model with grooving corrosion on the stiffener: (a) schematic diagram of the model cross-section; (b) weld connection details showing the FE node arrangement (where '×' represents the shared nodes).

Figure 5. Butt welded ship grade steel plate: Samples 1 to 4 in yellow frames are for the SKPFM test (25 mm × 25 mm × 6 mm).

Figure 6: Distribution of the anodic current density increment ratio i_a/i_{a0} for a plate with random pitting corrosion (DOP = 15%, pit depth = $0.2t$): (a) at $0.43\sigma_y$ top view; (b) at $0.65\sigma_y$ top view; (c) at $0.43\sigma_y$ pit cross-section; (d) at $0.65\sigma_y$ pit cross section (scale bars indicate i_a/i_{a0} ratio).

Figure 7: Results along line x = 400 mm for the plate model with a large corrosion feature in the middle at ultimate strength stage (DOP = 15%): (a) hydrostatic pressure (MPa); (b) equivalent plastic strain; (c) anodic current density increment ratio i_a/i_{a0}.

Figure 8: Anodic current density increment ratio i_a/i_{a0} along line x = 400 mm for plate model with a large corrosion feature in the middle at different load substeps (DOP = 15%): (a) pit depth = $0.25t$; (b) pit depth = $0.5t$.

Figure 9: Anodic current density increment ratio i_a/i_{a0} along line x = 400 mm for plate model with a large corrosion feature in the middle and various DOPs (pit depth = $0.25t$).

Figure 10: An intact stiffened plate with residual stresses in the longitudinal direction: (a) anodic current density increment ratio i_a/i_{a0} distribution; (b) longitudinal residual stress and total anodic potential change (summation of elastic and plastic effects) along line A-A' (from weld boundary to plate edge).

Figure 11: SKPFM measurements across the weldment and the base metal (Samples 1 to 4 in Figure 5).

Figure 12: Anodic current density increment ratio i_a/i_{a0} at different load substeps for a stiffened plate model with grooving corrosion on the stiffener (w_{gc} = 15%h_w; t_{gc} = $0.75t_w$).

Commented [Y.45]: Reviewer #3 Comment 4

Commented [Y.46]: Reviewer #3 Comment 4

Commented [Y.47]: Reviewer #3 Comment 5

Figure 13: Lines P_1-P_1' and P_2-P_2' of a stiffened plate model with grooving corrosion on the stiffener (w_{gc} = 10%h_w; t_{gc} = 0.75, 0.5 and 0.25t_w): (a) hydrostatic pressure; (b) equivalent plastic strain; (c) anodic current density increment ratio i_a/i_{a0}.The dashed lines indicate the location of the stiffener.

Figure 14: Line W_1-W_1' of a stiffened plate model with grooving corrosion (grey area) on the stiffener (w_{gc} = 10%h_w; t_{gc} = 0.75, 0.5 and 0.25t_w): (a) hydrostatic pressure; (b) equivalent plastic strain; (c) anodic current density increment ratio i_a/i_{a0}.

Figure 15: Line W_2-W_2' of a stiffened plate model with grooving corrosion (grey area) on the stiffener (w_{gc} = 10%h_w; t_{gc} = 0.75, 0.5 and 0.25t_w): (a) hydrostatic pressure; (b) equivalent plastic strain; (c) anodic current density increment ratio i_a/i_{a0}.

Figure 16: Equivalent plastic strain at the mid-section of stiffened plate model with grooving corrosion at the ultimate strength stage: (a) 0.75t_w and (b) 0.25t_w.

TABLE CAPTIONS

Table 1. Properties used for square plate and stiffened plate models

Table 1

Click here to download Table: Table 1.docx

Model Properties	Square plate model	Stiffened plate model
a / mm	800	4750
b / mm	800	950
t / mm	15	15
$h_w \times t_w$ / mm	-	235 × 12
$b_f \times t_f$ / mm	-	90 × 17
E / GPa	205.8	205.8 (both plate and stiffener)
σ_y / MPa	352.8	313.6 (both plate and stiffener)
ν	0.3	0.3 (both plate and stiffener)
E_t / GPa	0	0 (both plate and stiffener)
$\beta = \frac{b}{t}\sqrt{\frac{\sigma_y}{E}}$ (plate slenderness ratio)	2.208	2.472
Plate initial deflection / mm	$w_{pl} = 0.1\beta^2 t \sin\frac{\pi x}{a}\sin\frac{\pi y}{b}$	$w_{pl} = 0.1\beta^2 t \sin\frac{5\pi x}{a}\sin\frac{\pi y}{b}$
Column-type initial deflection / mm (B / mm: width between two longitudinal girders)	-	$w_c = 0.0015a \sin\frac{\pi x}{a}\sin\frac{\pi y}{B}$
Sideways initial deflection / mm	-	$w_s = 0.0015a \frac{z}{h_w}\sin\frac{\pi x}{a}$

Figure 1

Click here to download Figure: Figure 1.docx

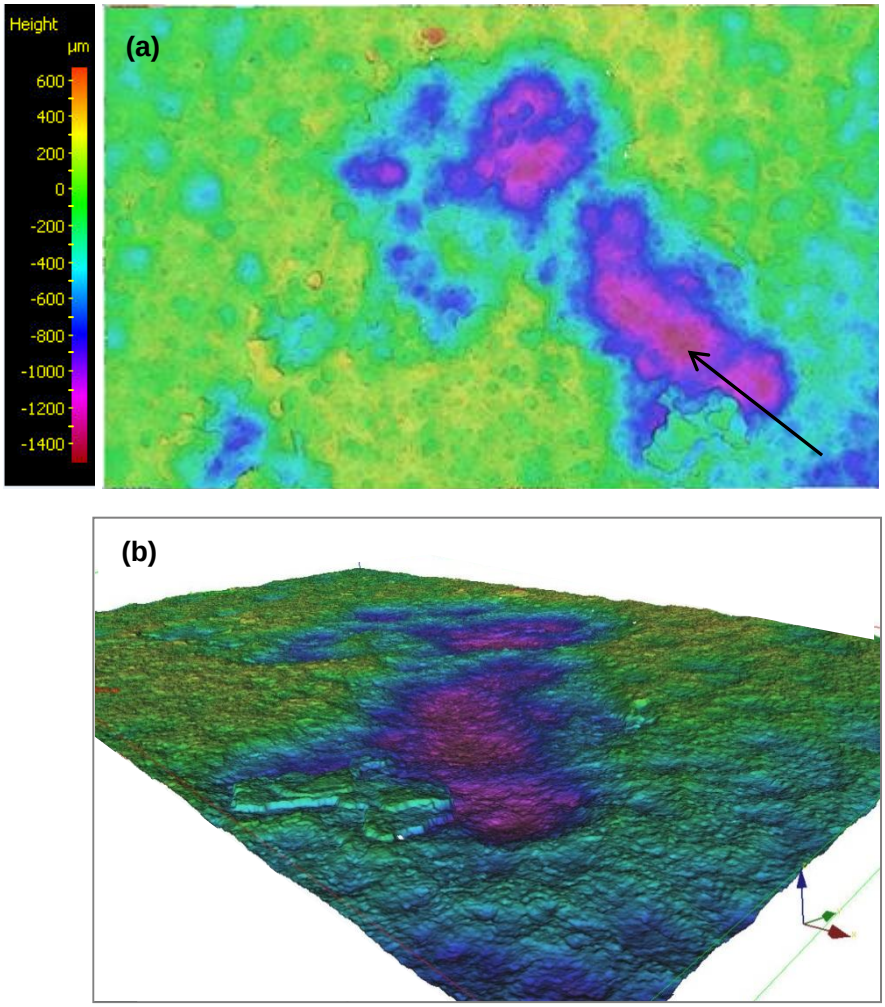

Figure 2

Click here to download Figure: Figure 2.docx

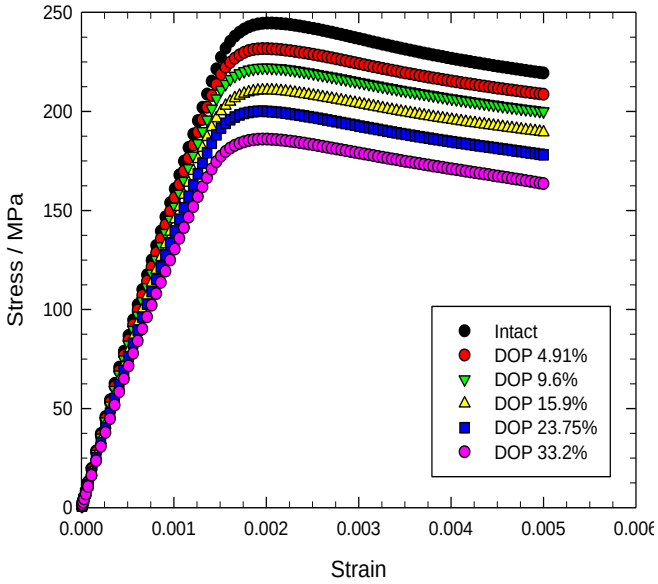

(a)

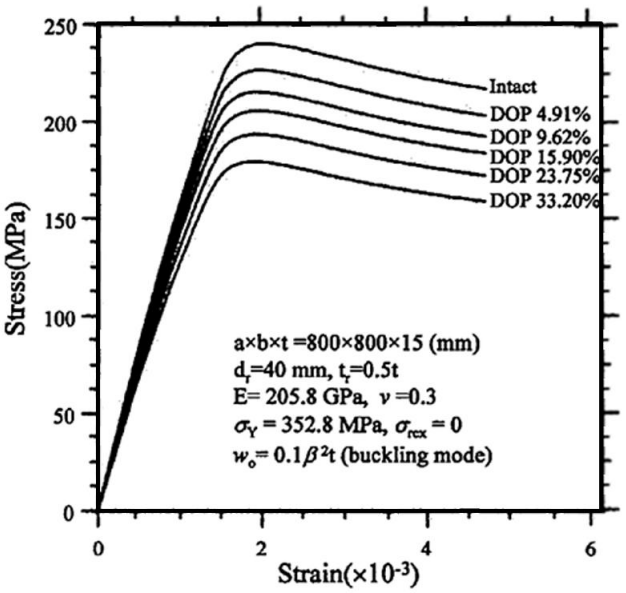

(b)

Figure 3

Click here to download Figure: Figure 3.docx

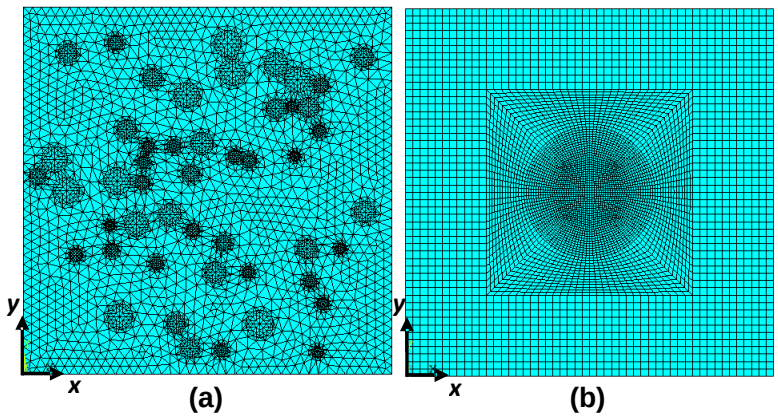

Figure 4

Click here to download Figure: Figure 4.docx

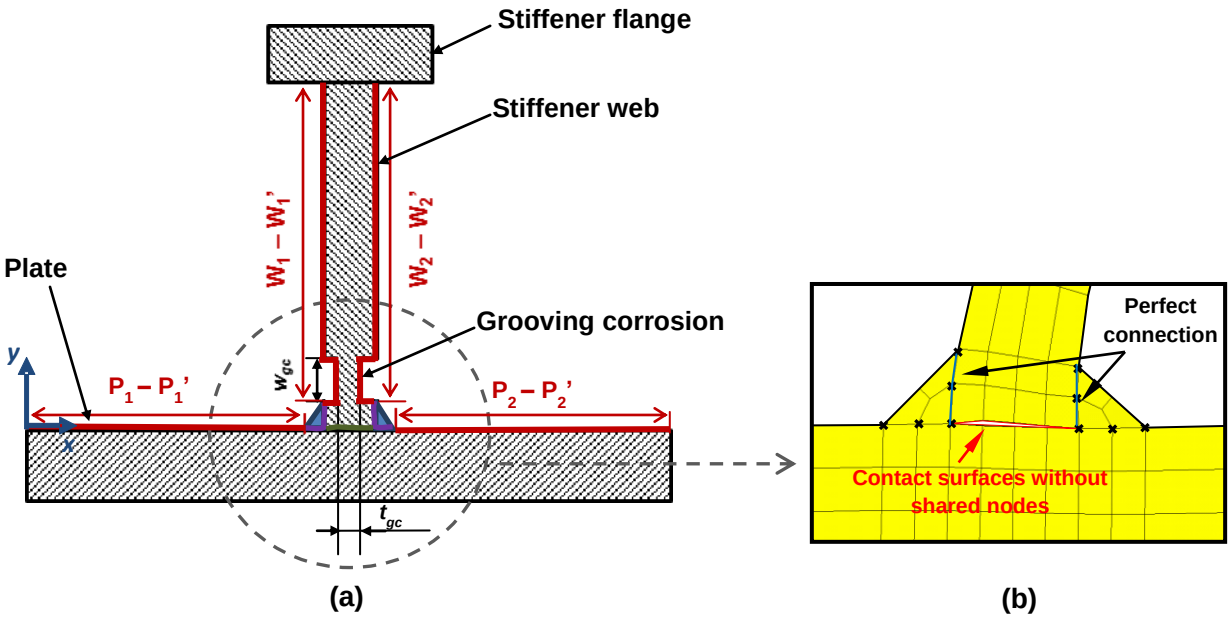

(a) (b)

Figure 5

Click here to download Figure: Figure 5.docx

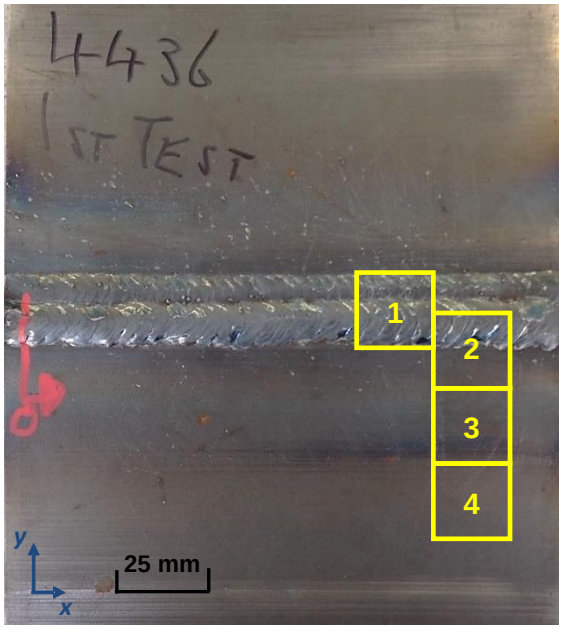

Figure 6

Click here to download Figure: Figure 6.docx

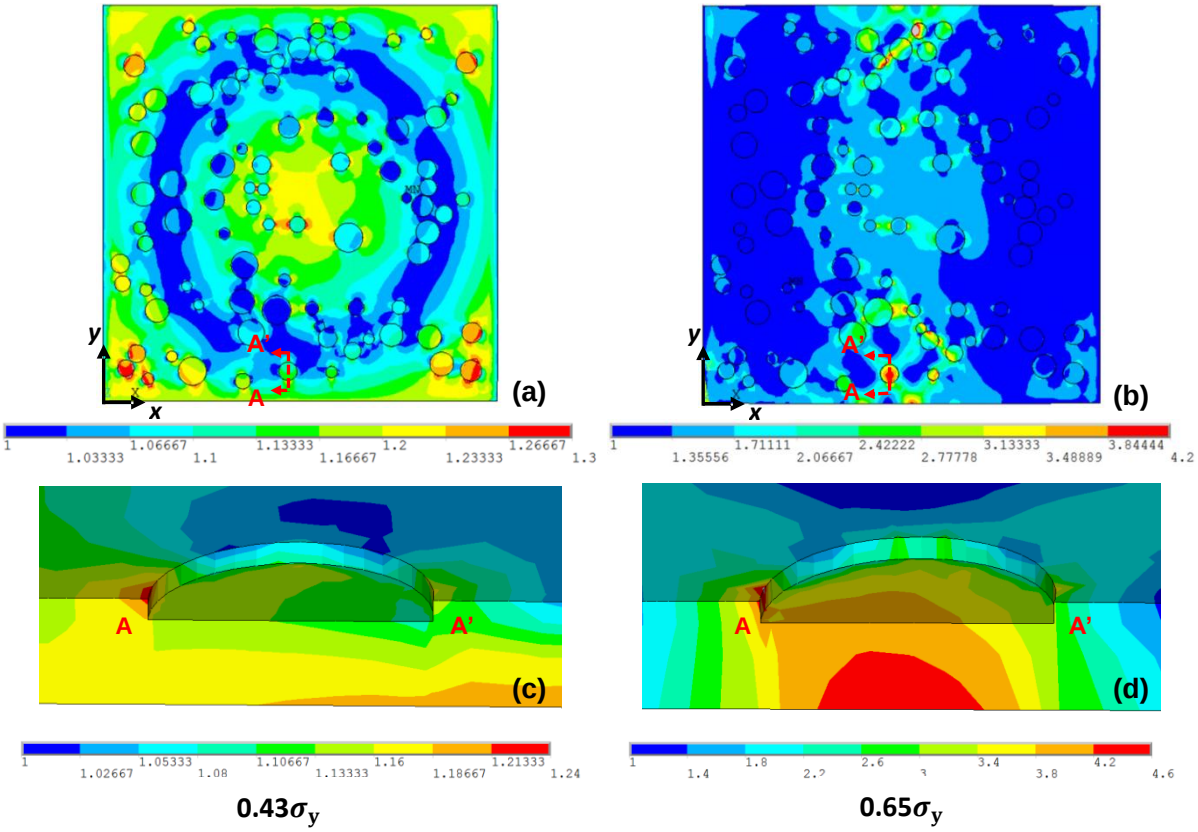

$0.43\sigma_y$ $0.65\sigma_y$

Figure 7

Click here to download Figure: Figure 7.docx

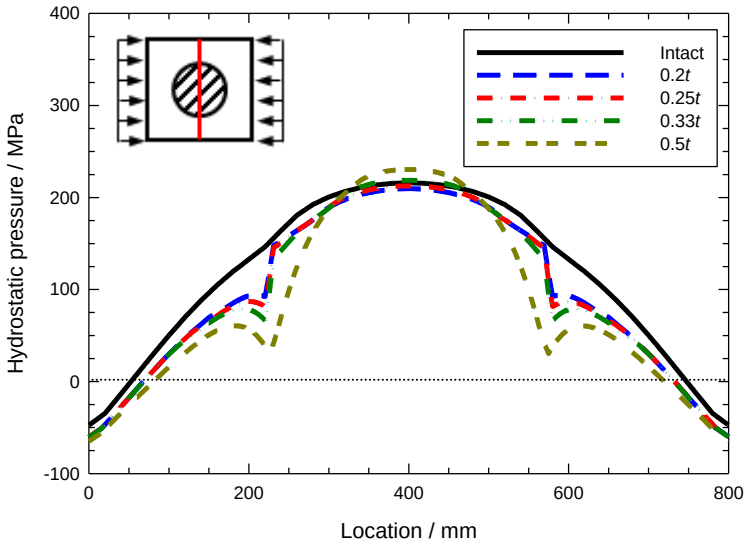

(a)

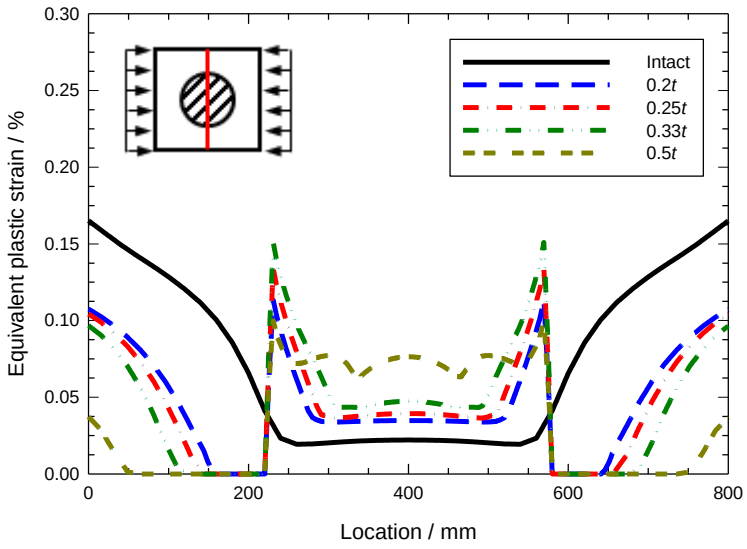

(b)

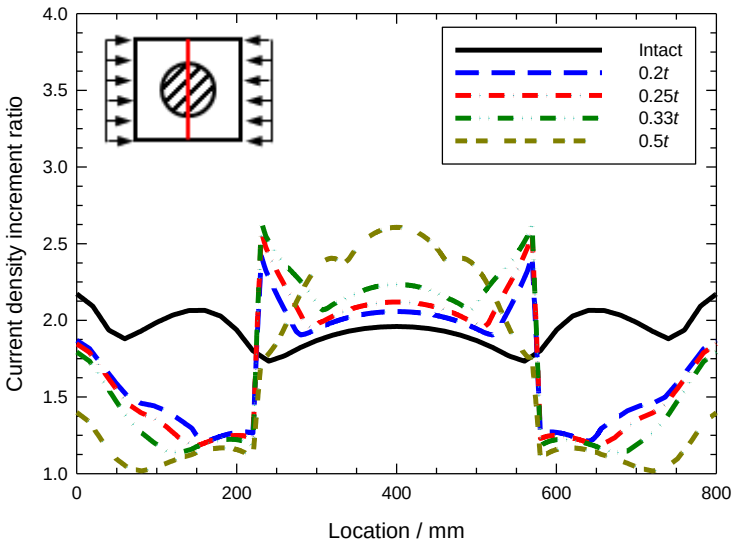

(c)

Figure 8

Click here to download Figure: Figure 8.docx

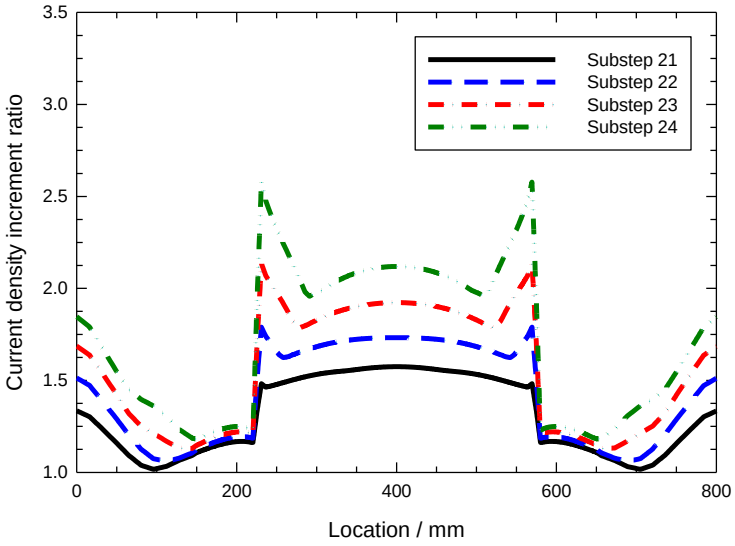

(a) DOP=15%, 0.25*t*

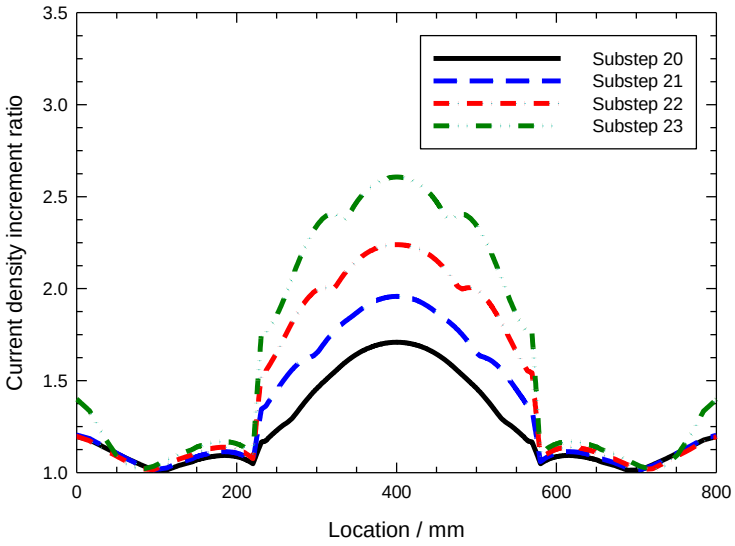

(b) DOP=15%, 0.5*t*

Figure 9

Click here to download Figure: Figure 9.docx

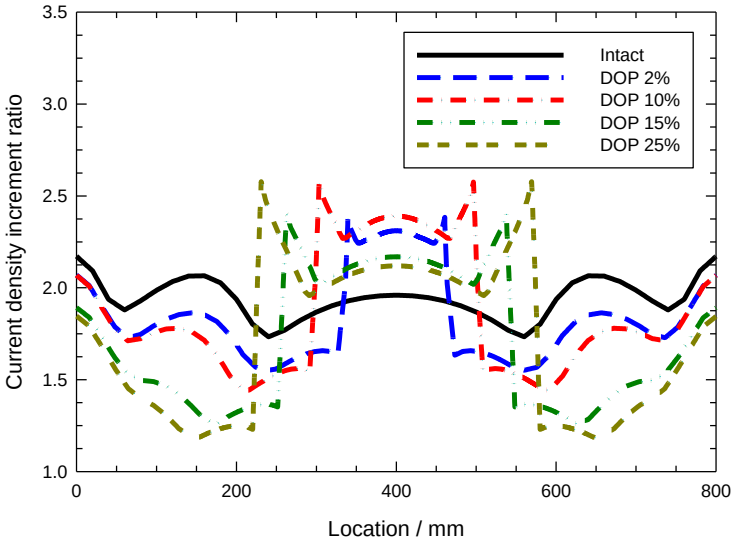

Figure 10

Click here to download Figure: Figure 10.docx

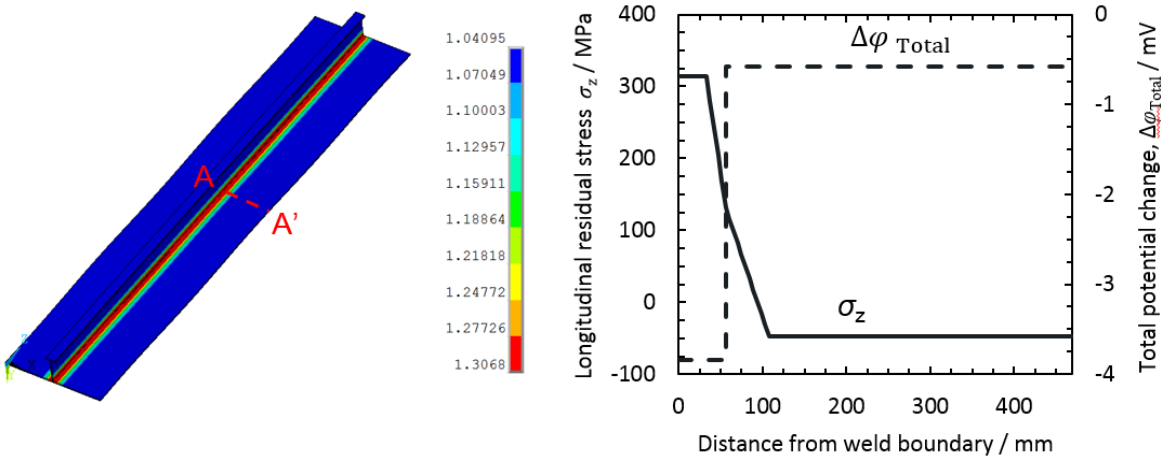

(a) **(b)**

Figure 11

Click here to download Figure: Figure 11.docx

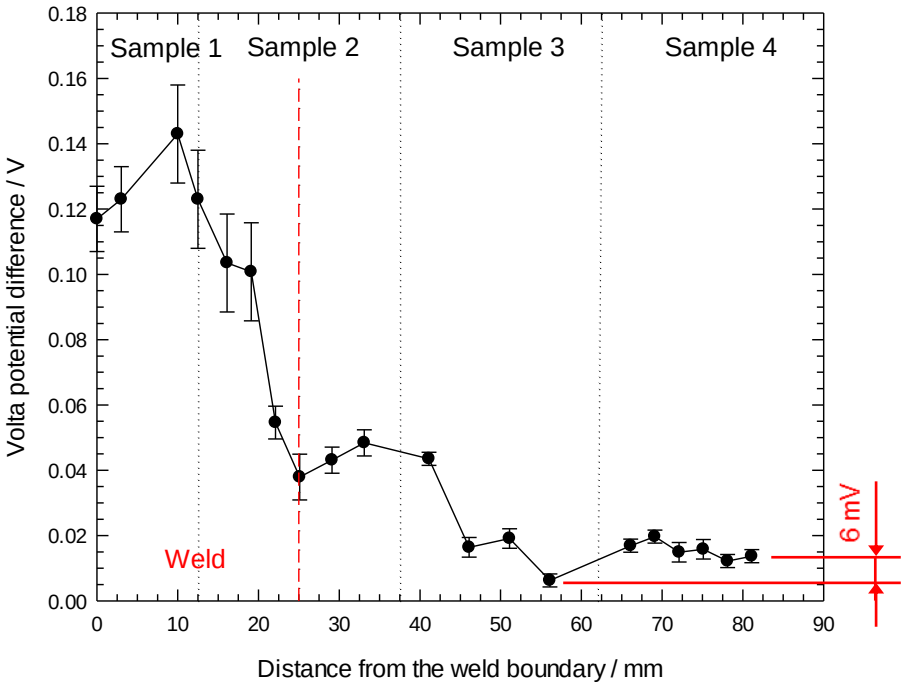

Figure 12

Click here to download Figure: Figure 12.docx

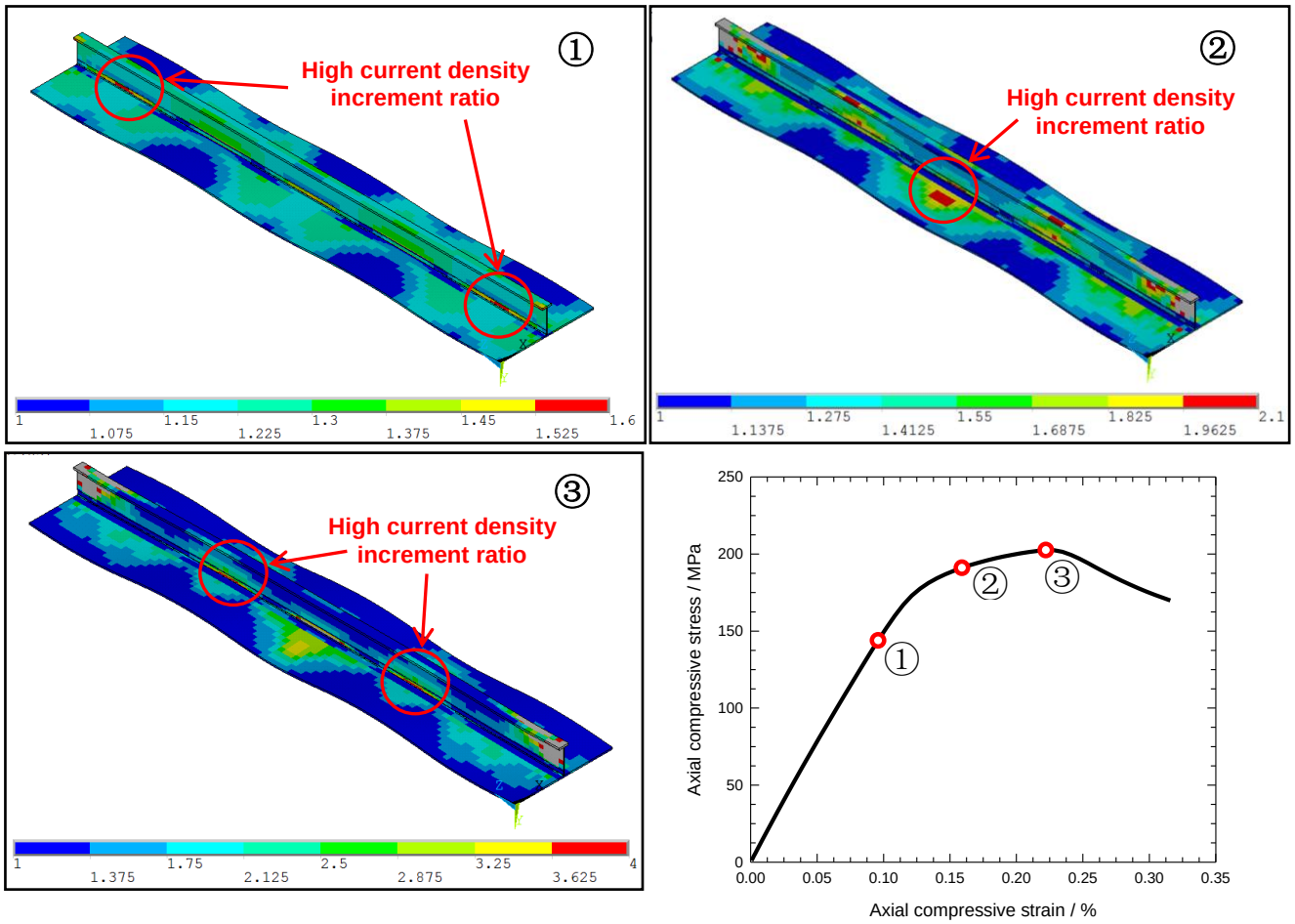

Figure 13

Click here to download Figure: Figure 13.docx

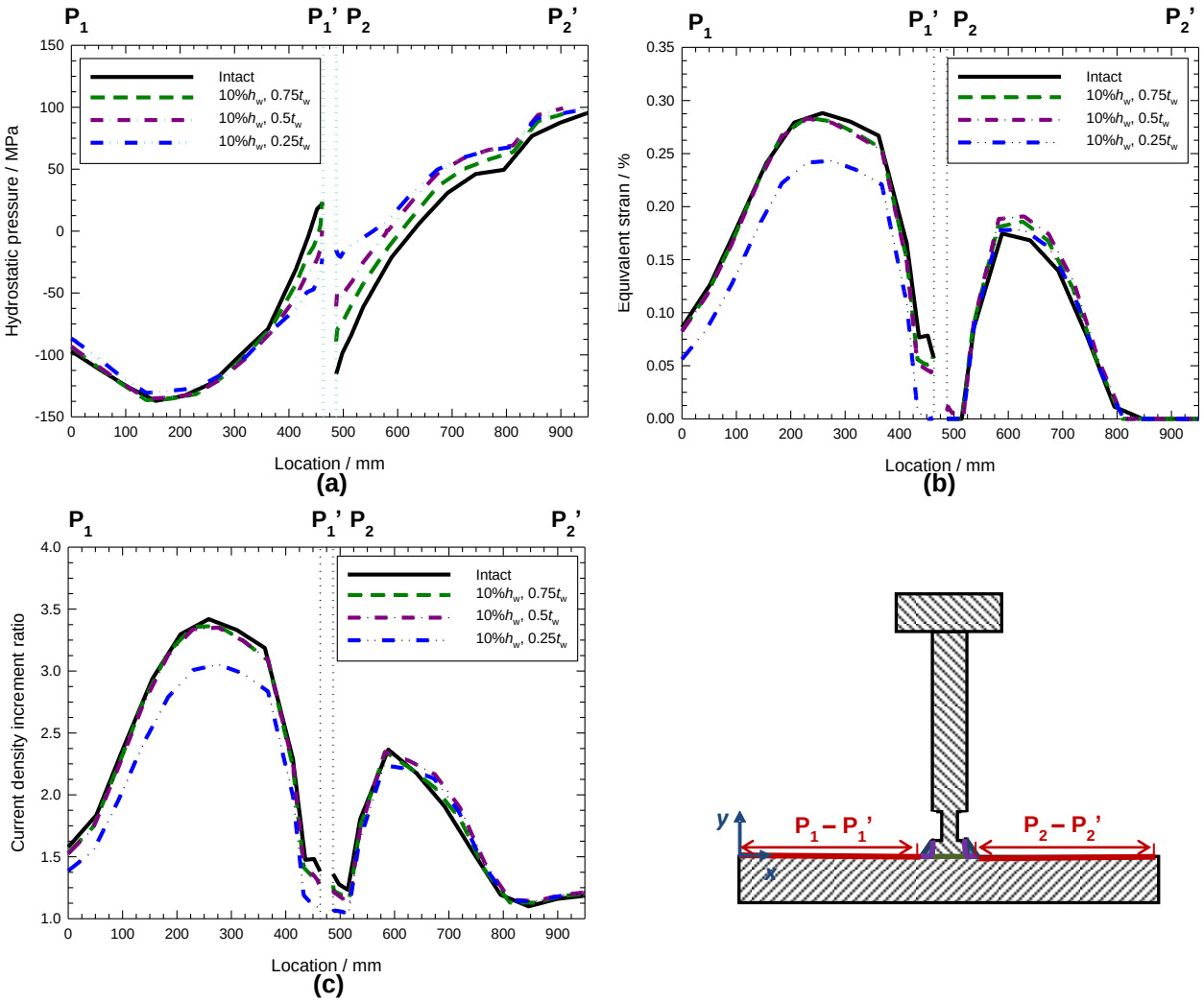

Figure 14

Click here to download Figure: Figure 14.docx

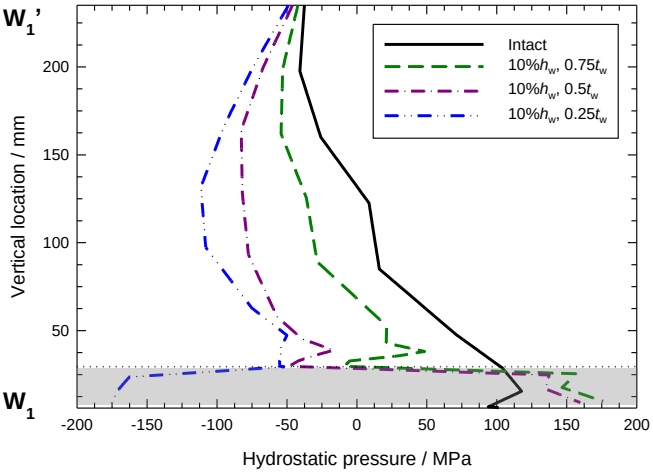

(a)

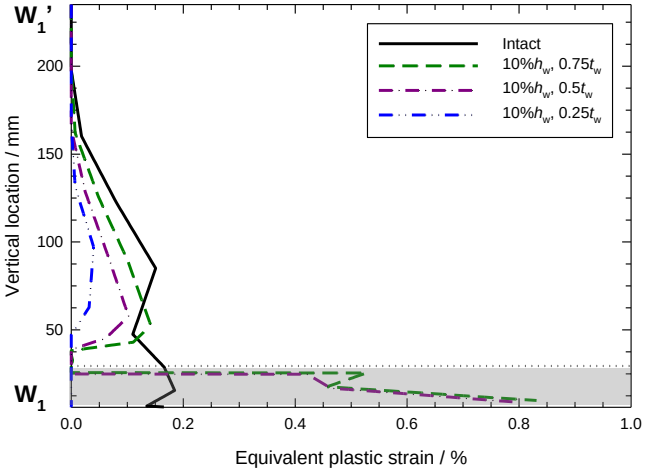

(b)

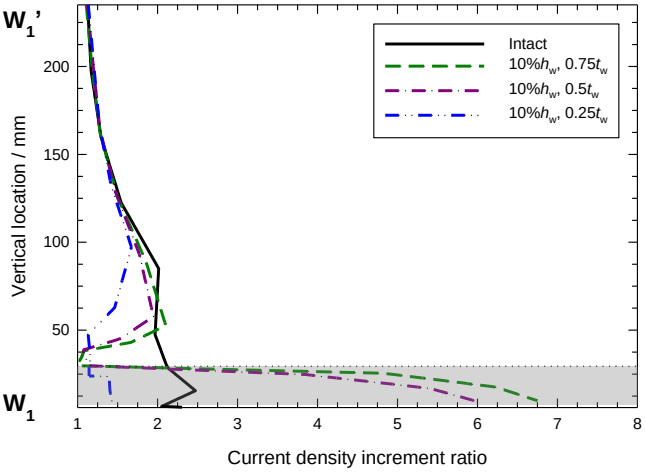

(c)

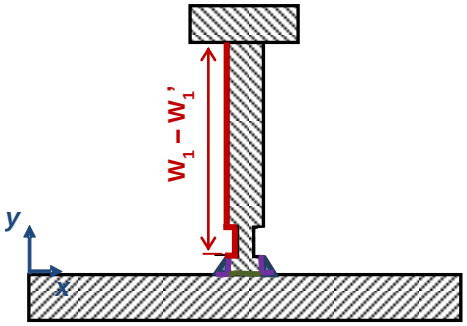

Figure 15

Click here to download Figure: Figure 15.docx

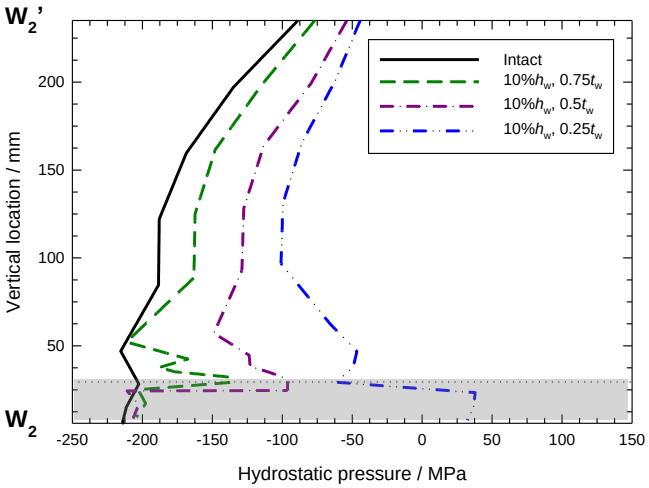

(a)

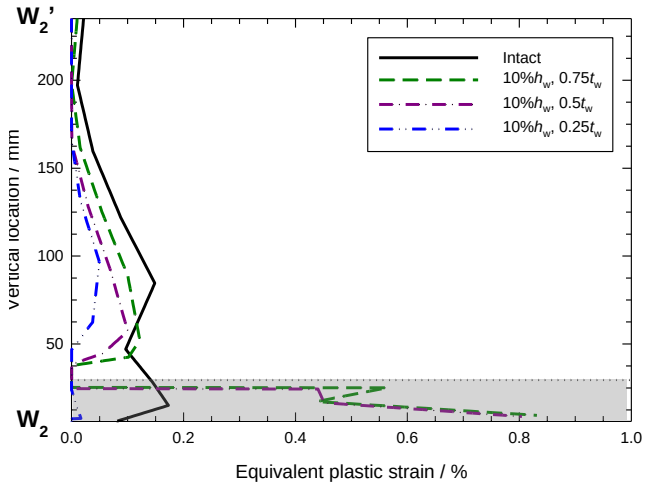

(b)

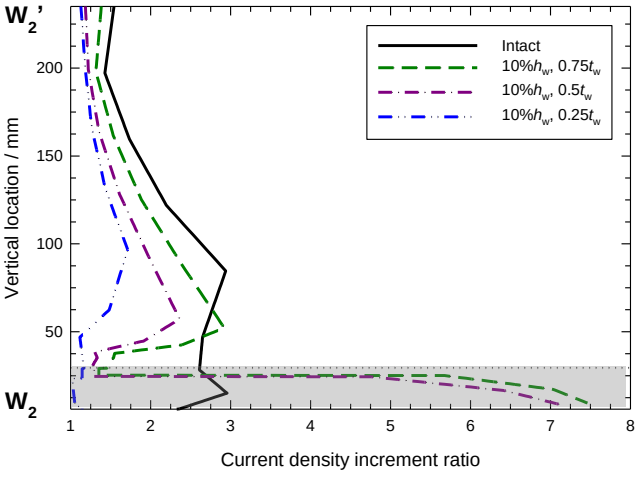

(c)

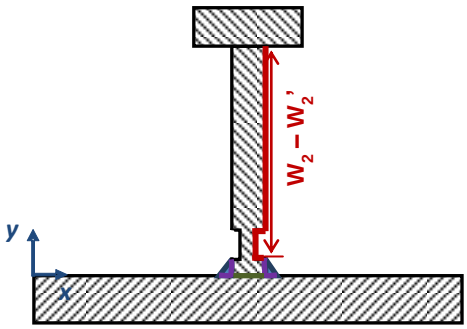

Figure 16

Click here to download Figure: Figure 16.docx

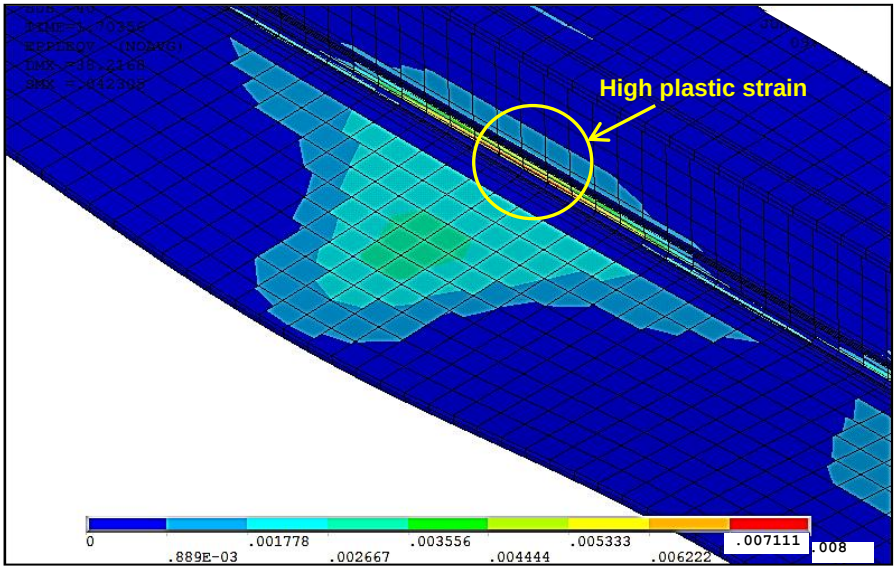

(a) 10%h_w–0.75t_w

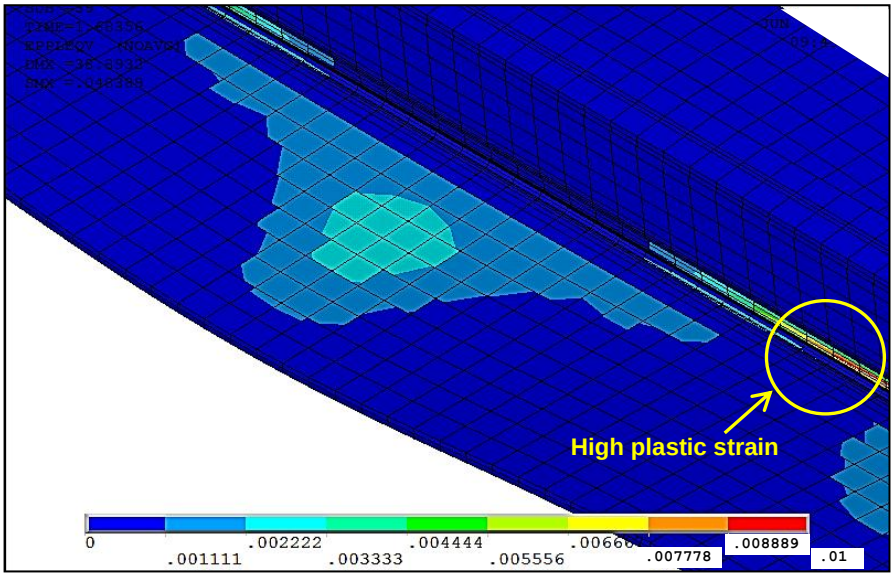

(b) 10%h_w–0.25t_w